



## Research paper

## CFD analysis and design of bypass dual throat nozzle for high-performance fluidic thrust vectoring

Chanho Park<sup>1</sup>, Woochan Lee<sup>1</sup>, Seongim Choi\**Gwangju Institute of Science and Technology, Department of Mechanical Engineering, Gwangju 61005, South Korea*

## ARTICLE INFO

## Keywords:

Bypass dual throat nozzle  
Sensitivity analysis  
Data-driven optimization

## ABSTRACT

The purpose of the study is to investigate detailed flow properties of the bypass dual throat nozzle (BDTN) for fluidic thrust vectoring, and to find an optimal geometry to maximize its performance. The performance metrics of the BDTN are defined as the thrust efficiency and flow deflection angle at the nozzle exit. Given the nozzle pressure ratio (NPR), secondary flows injected from the bypass duct of the nozzle create circulatory flows in the nozzle cavity, produce complex interactions of shock and expansion waves, and deflect the directions of the exit flows. To identify key parameters for the BDTN performance, a sensitivity study is carried out using the traditional finite difference method as well as the AI-assisted Shapley additive explanation methods with respect to geometric variables of the BDTN. For the design optimization, a total of eight geometric parameters were chosen including an upstream convergent angle ( $\theta_1$ ), a bypass injection angle ( $\theta_2$ ), cavity divergence and convergence angles ( $\theta_3$  and  $\theta_4$ ), upstream and downstream throat diameters ( $d_2$  and  $d_3$ ), bypass channel diameter ( $d_4$ ), and cavity divergence length ( $l_1$ ). Those parameters were varied by 10~20 % of the baseline values to create more than 100 random BDTN geometries which were solved by the full CFD analysis. The multi-variate Gaussian process regression (GPR) model was developed by training the data as a surrogate model to the CFD analysis of arbitrary BDTN shape during the design iteration. Multi-objective optimization was conducted to generate the Pareto optimal front of multiple design candidates for maximum deflection angle and thrust values. The optimum BDTN geometry produced a deflection angle increased up to 13 %, while thrust value was slightly increased from that of the baseline by less than 1%. The approach provides a foundation for future research into adaptive nozzle designs responsive to real-time flow conditions, potentially expanding the applications of fluidic thrust vectoring.

## 1. Introduction

Highly agile flight capabilities remain a crucial attribute for fighters from the past to the future [1,2]. A fighter jet with superior agility often holds the upper hand in aerial dogfights. One key element that enhances this agility is the thrust vectoring nozzle. For instance, the American F-22 fighter uses a rectangular exit thrust vectoring nozzle to create pitch moments [3,4]. However, Mechanical Thrust Vectoring (MTV) has limitations due to its complex structure, high maintenance costs, and inefficient aerodynamic characteristics [5–7]. In contrast, Fluidic Thrust Vectoring (FTV), which operates without dynamic parts, has a relatively simple structure, making maintenance more manageable. Additionally, it is aerodynamically efficient and emits a lower Infrared (IR) signal, resulting in superior stealth capabilities compared to MTV [8–10].

There are three main types of Fluidic Thrust Vectoring (FTV): the first is Shock Vector Control (SVC), the second is counterflow, and the

third is throat skewing. Shock Vector Control, operates by generating bow shock waves when the supersonic main nozzle flow interacts with a secondary injection flow, which acts as an obstruction [11–13]. This shock wave deflects the main nozzle flow by altering its trajectory. The most effective thrust vectoring performance with SVC is achieved when the over-expanded nozzle flow's separation on one wall is eliminated by an inclined shock wave, creating a pressure differential across the nozzle walls. However, SVC faces limitations, including reduced thrust efficiency due to the need to maintain over-expansion conditions and reliance on shock waves for effective thrust deflection [14,15]. Counterflow thrust vectoring nozzles also use Laval nozzles as a baseline but include an intake, which operates at vacuum pressure, and an exhaust, which directs flow in the same direction as the main nozzle, allowing the flow to deflect [16]. However, experimental studies identified the primary issue as the tendency of the main flow to attach to the intake flow, exhibiting hysteretic behavior,

\* Corresponding author.

E-mail address: [schoi1@gist.ac.kr](mailto:schoi1@gist.ac.kr) (S. Choi).

† Co-lead author.

which makes it difficult to control [17,18]. The Throat Skewing (or Throat Shifting) method also employs Laval nozzles, but unlike SVC, it leverages pressure differentials caused by asymmetric flow separation, rather than shock waves, to achieve thrust vectoring [19,20]. In this method, the secondary injection is positioned at the nozzle throat, the area of minimum flow cross-section, rather than in the diverging section as in SVC.

Dual Throat Nozzles (DTNs) represent an evolution of the throat skewing method, adding a converging section to more effectively harness flow separation [21–23]. This design creates a cavity region where the secondary injection expands the flow separation area, leading to a stronger asymmetric pressure differential that induces thrust vectoring [24–26]. Consequently, extensive parameter studies have been conducted on DTNs. Flamm et al. [27] carried out experimental parameter studies on DTNs with 3-D and axisymmetric configurations, examining aspects such as injection rate, thrust, mass flow, and deflection efficiency. Similarly, Deere et al. [28] conducted numerical parameter studies using Computational Fluid Dynamics (CFD) on axisymmetric DTNs. Building on the foundational DTN concept, the Bypass Dual Throat Nozzle (BDTN), first invented by [29], offers further advancements in thrust vectoring. The BDTN eliminates the need for secondary injection by redirecting the primary flow through a bypass channel, reintroducing it at the throat section to achieve vectoring (see Fig. 1). This refined approach minimizes the pressure losses typically associated with secondary flow injection, while still maximizing the vectoring angles [30–34]. Consequently, BDTNs have garnered attention for their ability to enhance thrust vectoring performance with minimal thrust loss, prompting ongoing research and development in this area.

Pan et al. [35] aimed to reduce the infrared (IR) signal and decrease detectability by enhancing the mixing of the flow through tab modification. Additionally, Huang et al. [36] conducted an investigation to verify the potential of improving the mixing performance through nozzle shape modification. They extended their study of BDTNs with rectangular cross-sections by developing a novel BDTN design that features trapezoidal cross-sections, modifying each cross-section from a rectangle to a trapezoid. Huang et al. [37] also researched the possibility of extending the capability for Short/Vertical Take-Off and Landing (S/VTOL) by modifying part of the BDTN shape using a rotational shaft, utilizing phenomena such as the Coanda effect for application in S/VTOL systems. Kim et al. [38] demonstrated that by utilizing the unique shape of the BDTN nozzle, it is possible to achieve sufficient deflection angles without bending to 90 degrees, as is typically required in mechanical vectoring. This was confirmed by showing that the deflection efficiency is superior when the duct of the nozzle is bent, compared to a conventional nozzle shape.

Moreover, studies on the performance of BDTNs based on shape parameters have been actively conducted. Hamed-Estakhsar et al. [39] studied the performance of BDTN nozzles as a function of the bypass channel area. Wang et al. [40,41] compared performance based on the expansion ratio, the degree of shape smoothing, and the bypass channel area for a 3D axisymmetric divergent BDTN. Additionally, to evaluate the controllability of the BDTN, research has been conducted on adjusting the throat and exit area of the nozzle mechanically to observe the flow fields and performance. Wu and Kim [42] explored the potential for performance improvement by examining the flow fields and performance of a nozzle with an arc-shaped bypass channel designed to minimize pressure loss. Following this, Huang et al. [43] also compared the performance of various bypass channel shapes to find the optimal design under different NPR (Nozzle Pressure Ratios) and valve opening levels.

Despite the significance of BDTN nozzles, the high computational costs have limited the scope of parameter studies, preventing thorough optimization efforts. Shape optimization for performance maximization remains a challenging task due to complexities in shape parameterization, mesh deformation, physics-based numerical analysis, and optimization algorithms. One of the major hurdles is the computational

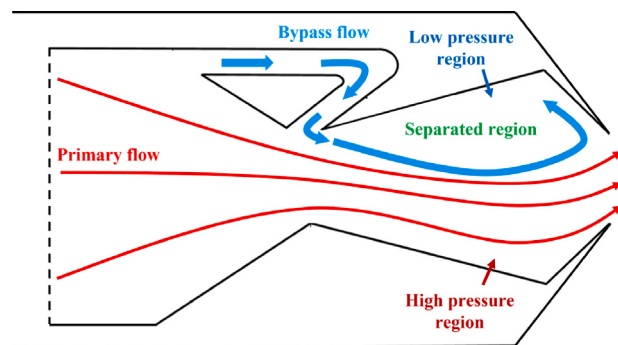


Fig. 1. Sketch of the Bypass Dual Throat Nozzle (BDTN).

cost involved in solving these physics-based problems repeatedly to evaluate the performance of design candidates whose shapes have been modified from the initial baseline. Even with the use of high-performance computers and advanced numerical methods, the overall cost can render the design process impractical.

To address these challenges, we aim to systematically set shape parameters and conduct a sensitivity analysis to identify the key factors that influence performance. By optimizing these parameters, we seek to develop an efficient, cost-effective approach to shape optimization. Therefore, we aim to extend the previous research on DTN shape optimization [44] and apply shape optimization to BDTNs through machine learning, significantly reducing computational costs. Initially, we will use a classical FDM-based parameter study to understand how nozzle performance and flow fields – such as shocks and sonic lines inside the nozzle – change with the shape parameters. This will allow us to identify key parameters that affect nozzle performance. Furthermore, by incorporating eXplainable Artificial Intelligence (XAI), we will consider the nonlinear interactions between variables and clarify the contributions of each parameter, improving the accuracy of shape optimization and enabling efficient analysis even with high-dimensional data. We will then use Gaussian Process Regression (GPR) to build a surrogate model, and employ a Genetic Algorithm to identify the Pareto front, which represents the optimal shapes that provide the best performance.

The structure of the paper is as follows. Section 2 presents the methodology, including compressible RANS solver with turbulence model. Section 3 details the validation of the full CFD analysis, shape parameterization of the BDTN nozzle, and the sensitivity analysis of the BDTN performance. Section 4 describes the optimization process and design results. Finally, Section 5 consolidates the findings and outlines future research directions.

## 2. Methodology

### 2.1. Computational methods

#### 2.1.1. Governing equations

The Realizable  $k-\epsilon$  model has been widely used in studies related to fluidic thrust vectoring due to its high accuracy and reliability in complex flow fields under high Reynolds number conditions, as it effectively captures key flow characteristics such as separation, recirculation, and shear layer effects, which are critical in predicting thrust coefficient accurately [32,36,37,45]. Prior research [29] validated the reliability of the Realizable  $k-\epsilon$  model by comparing experimental results with CFD simulations for the baseline Bypass Dual Throat Nozzle (BDTN), demonstrating its suitability for similar applications. Additionally, the same study compared 2D and 3D simulation results, showing that 2D simulations accurately reproduced the internal flow field structures of the nozzle while significantly reducing computational costs

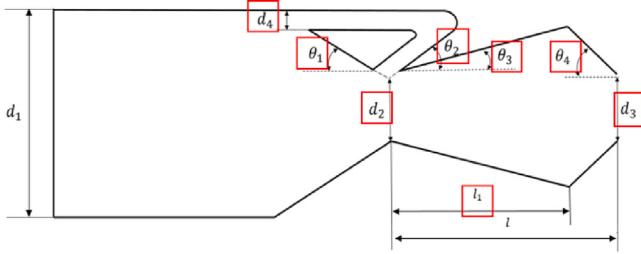


**Fig. 2.** Geometric parameters of the BDTN used in the sensitivity analysis and optimization studies.

compared to 3D models. Specifically, the differences in thrust ratio and thrust vectoring angle between 2D and 3D results were within 1%, proving that the 2D model can reliably and efficiently predict the key flow characteristics and performance of the BDTN.

Building on this foundation, the Realizable  $k-\epsilon$  model and 2D simulation are employed in this study for the 2D, steady, and compressible RANS simulation to analyze the flow field characteristics.

The transport equations for the turbulence kinetic energy  $k$  and the dissipation rate  $\epsilon$  in the Realizable  $k-\epsilon$  model are:

$$\frac{\partial}{\partial t}(\rho k) + \frac{\partial}{\partial x_j}(\rho k u_j) = \frac{\partial}{\partial x_j} \left[ \left( \mu + \frac{\mu_t}{\sigma_k} \right) \frac{\partial k}{\partial x_j} \right] + G_k + G_b - \rho \epsilon - Y_M + S_k \quad (1)$$

$$\begin{aligned} \frac{\partial}{\partial t}(\rho \epsilon) + \frac{\partial}{\partial x_j}(\rho \epsilon u_j) &= \frac{\partial}{\partial x_j} \left[ \left( \mu + \frac{\mu_t}{\sigma_\epsilon} \right) \frac{\partial \epsilon}{\partial x_j} \right] \\ &+ C_1 \frac{\epsilon}{k} (G_k + C_3 G_b) - C_2 \rho \frac{\epsilon^2}{k + \sqrt{\nu \epsilon}} + S_\epsilon \end{aligned} \quad (2)$$

In these equations,  $G_k$  is the generation of turbulence kinetic energy due to mean velocity gradients, and  $G_b$  represents buoyancy effects.  $Y_M$  accounts for the contribution of compressibility, and  $S_k$  and  $S_\epsilon$  are user-defined source terms.

The Realizable  $k-\epsilon$  model ensures that the normal stresses remain positive under large strain rates. This is achieved by enforcing the following condition on the strain rate:

$$\frac{k}{\epsilon} \frac{\partial U}{\partial x} > \frac{1}{3C_\mu} \approx 3.7 \quad (3)$$

This condition prevents non-realizable states in which the turbulence model would predict physically impossible results.

The turbulent eddy viscosity  $\mu_t$  is computed as:

$$\mu_t = \rho C_\mu \frac{k^2}{\epsilon} \quad (4)$$

In the realizable  $k-\epsilon$  model,  $C_\mu$  is no longer treated as a constant but is instead dynamically computed based on the local flow conditions.

$C_\mu$  is calculated as:

$$C_\mu = \frac{1}{A_0 + A_s \frac{kU^*}{\epsilon}} \quad (5)$$

where  $U^* = \sqrt{S_{ij}S_{ij} + \tilde{\Omega}_{ij}\tilde{\Omega}_{ij}}$ , with  $S_{ij}$  and  $\tilde{\Omega}_{ij}$  being the mean strain-rate and rotation-rate tensors, respectively.  $A_0$  and  $A_s$  are model constants.

### 2.1.2. Shape configuration and computation setup

The nozzle shape parameters are illustrated in Fig. 2. For the sensitivity analysis and optimization of the nozzle, eight parameters were selected: the upstream convergent angle ( $\theta_1$ ), bypass injection angle ( $\theta_2$ ), cavity divergence angle ( $\theta_3$ ), cavity convergence angle ( $\theta_4$ ), height of the upstream throat area ( $d_2$ ), height of the downstream throat area ( $d_3$ ), height of the bypass duct area ( $d_4$ ), and length of the cavity divergence ( $l_1$ ). The height of the nozzle inlet ( $d_1$ ) is fixed, while the cavity length ( $l$ ) is dependent on other parameters.

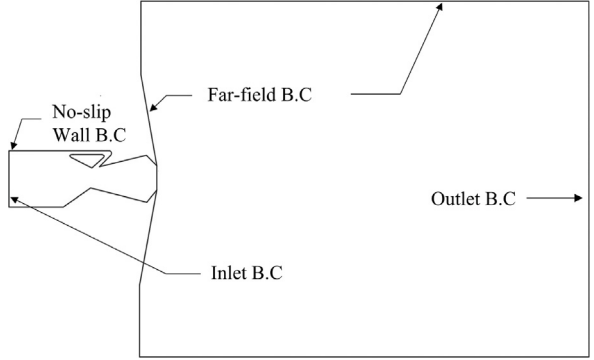


**Fig. 3.** Boundary conditions and computational domain setup for the BDTN simulations.

For the sensitivity analysis using a classic finite difference method (FDM), the selected eight parameters were varied from the baseline, with angles adjusted by  $\pm 20\%$  and lengths by  $\pm 10\%$  [29]. These values are summarized in Table 1.

The boundary conditions and computational domain are shown in Fig. 3. The outlet boundary condition (B.C.) was set as a pressure outlet boundary, with the pressure set to 101,325 Pa, the same as the far-field atmospheric pressure. For the inlet boundary condition, the pressure was set to 303,975 Pa to achieve a nozzle pressure ratio (NPR) of 3 relative to atmospheric pressure. The no-slip wall boundary condition was defined as an isothermal wall, with the temperature set to 300 K, matching the total temperature of inlet flow.

The far-field boundaries in the lateral directions are located at a distance equal to 30 times the height of the nozzle inlet from the center of the nozzle exit. The pressure outlet boundary is positioned 60 times the height of the nozzle inlet downstream from the center of the nozzle exit.

### 2.2. Explainable artificial intelligence (XAI)

In this study, we use SHAP (SHapley Additive exPlanations) to quantify the sensitivity of the eight shape parameters of the BDTN nozzle on the objective function. By computing the Shapley values, we can identify the contribution of each shape parameter to the model prediction, providing a rigorous explanation of their individual effects [46].

For each shape parameter  $i$ , its Shapley value  $\phi_i$  is calculated as follows:

$$\phi_i(f) = \sum_{S \subseteq N \setminus \{i\}} \frac{|S|!(|N| - |S| - 1)!}{|N|!} (f(S \cup \{i\}) - f(S)), \quad (6)$$

where  $N$  is the set of all shape parameters,  $S$  is a subset of shape parameters not containing  $i$ ,  $f(S)$  is the model's prediction when only the parameters in subset  $S$  are considered, and  $|S|$  is the size of the subset  $S$ .

This equation determines the marginal contribution of each shape parameter to every possible subset of the remaining parameters, weighted by the size of the subset. The sum of these contributions represents the overall impact of parameter  $i$  on the objective function.

The objective function  $f(x)$ , which is influenced by the eight shape parameters of the BDTN nozzle, can be decomposed as

$$f(x) = \phi_0 + \sum_{i=1}^8 \phi_i, \quad (7)$$

where  $\phi_0$  is the average model prediction (the baseline prediction),  $\phi_i$  is the Shapley value for shape parameter  $i$ , representing its contribution to the overall prediction, and the sum of the Shapley values  $\sum_{i=1}^8 \phi_i$  yields the total prediction for the objective function.

**Table 1**  
Nozzle shape parameters and their ranges.

Parameter	$\theta_1$ [deg]	$\theta_2$ [deg]	$\theta_3$ [deg]	$\theta_4$ [deg]	$d_2$ [mm]	$d_3$ [mm]	$d_4$ [mm]	$l_1$ [mm]
Baseline	30.0	44.788	14.788	50.0	20.0	24.0	3.7	55.950
Min	24.0	35.830	11.830	40.0	18.0	21.6	3.33	50.355
Max	36.0	53.746	17.746	60.0	22.0	26.4	4.07	61.545

The SHAP method ensures that the contributions of individual shape parameters sum to the total prediction, allowing us to understand the relative importance of each parameter in determining the objective function's value.

### 2.3. Gaussian process regression (GPR)

A Gaussian process regression (GPR) model, also called a Kriging model, is a supervised learning technique for function interpolation at untested input and is controlled by the mean and covariance kernel [47]. In order to estimate the function output response at the untested input parameter (in our case,  $a(x_i)$ ), the GPR model selects the function that best represents the training data from a set of possible functions. (see Eq. (8)~Eq. (10))

$$\mathbf{q}'^T = [\mathbf{q}'(\mathbf{x}_1)^T, \dots, \mathbf{q}'(\mathbf{x}_m)^T]^T \sim \mathcal{MGP}(\mathbf{m}(\mathbf{x}), \mathbf{k}(\mathbf{x}, \mathbf{x}')) \quad (8)$$

$$\begin{aligned} \mathcal{MGP}(\mathbf{x}; \mathbf{m}, \mathbf{K}) &= \frac{1}{(2\pi)^{r/2} |\mathbf{K}|^{1/2}} \\ &\times \exp\left(-\frac{1}{2}(\mathbf{x} - \mathbf{m})^T \mathbf{K}^{-1} (\mathbf{x} - \mathbf{m})\right) \end{aligned} \quad (9)$$

$$\mathbf{m}(\mathbf{x}) = \mathbb{E}[\mathbf{q}'(\mathbf{x})] \quad (10)$$

$$k(\mathbf{x}, \mathbf{x}') = \exp\left(-\gamma \|\mathbf{x} - \mathbf{x}'\|^2\right) \quad (11)$$

Where  $\mathbf{m}(\cdot)$  and  $k(\cdot, \cdot)$  represent the mean vector and covariance matrix of the data, respectively. In this study, a multivariate Gaussian model was employed because the modal coefficients, which are the output values of the model, are multi-dimensional. Specifically, the RBF covariance function was chosen as an empirical method (Eq. (11)), as it can transform non-linear patterns in the data into linearly separable patterns in a high-dimensional space. Once the covariance function is defined, a maximum likelihood estimation is carried out to determine the appropriate hyperparameters (Eq. (12)).

$$\log p(\mathbf{q}' | \mathbf{x}) = -\frac{1}{2}\mathbf{q}'^T \mathbf{K}^{-1} \mathbf{q}' - \frac{1}{2} \log |\mathbf{K}| - \frac{n}{2} \log 2\pi \quad (12)$$

Through this GPR, the nonlinear patterns in the data can be linearly separated in a higher-dimensional space, enabling the creation of a surrogate model.

## 3. Validation and sensitivity analysis

### 3.1. Performance metrics of BDTN simulation

Two performance coefficients were used to optimize the nozzle shape. The first is the thrust ratio ( $C_f$ ), which is related to the nozzle thrust. The second is the thrust vectoring efficiency ( $\delta$ ), which is related to the nozzle's deflection efficiency. The thrust ratio  $C_f$  is expressed by the following equation:

$$C_f = \frac{F_r}{F_i} \quad (13)$$

where  $F_r = \sqrt{F_A^2 + F_N^2}$ , with  $F_A$  being the nozzle's axial force and  $F_N$  being the nozzle's normal force.  $F_i$  is expressed by the following equation:

$$F_i = \dot{m}_a \sqrt{\frac{2\gamma}{\gamma-1} RT_0} \left( 1 - \left( \frac{P_{\text{atm}}}{P_0} \right)^{\frac{\gamma-1}{\gamma}} \right) \quad (14)$$

**Table 2**  
Grid resolution study for NPR = 3.

NPR = 3	No. of cells	Relative error [%]	
		$C_f$	$\delta$
Coarse	$3.3 \times 10^4$	0.930	4.471
Medium	$4.9 \times 10^4$	0	0
Fine	$8.0 \times 10^4$	0.139	0.073

where  $\dot{m}_a$  is the actual mass flow rate at the nozzle inlet,  $R$  is the specific gas constant,  $\gamma$  is the specific heat ratio,  $T_0$  is the nozzle inlet total temperature,  $P_{\text{atm}}$  is the atmospheric pressure, and  $P_0$  is the nozzle inlet total pressure. Hence,  $P_{\text{atm}}/P_0$  represents the NPR.

The ideal mass flow rate  $\dot{m}_i$  is given by:

$$\dot{m}_i = A_t P_0 \left( \frac{2}{\gamma+1} \right)^{\frac{\gamma+1}{2(\gamma-1)}} \sqrt{\frac{\gamma}{T_0 R}} \quad (15)$$

where  $A_t$  is the nozzle throat area.

The thrust vectoring efficiency  $\delta$  is expressed as follows:

$$\delta = \tan^{-1} \left( \frac{F_N}{F_A} \right) \quad (16)$$

Here,  $F_N$  and  $F_A$  can be obtained by the following equations:

$$F_A = \int_{A_{\text{exit}}} (\rho v_{x,\text{exit}}^2 + (P_{\text{exit}} - P_{\text{atm}})) dA \quad (17)$$

$$F_N = \int_{A_{\text{exit}}} (\rho v_{x,\text{exit}} v_{y,\text{exit}}) dA \quad (18)$$

The optimization problem can therefore be formulated as follows.

$$\operatorname{argmax}_{\mathbf{x}} f(\mathbf{x}) = [C_f(\mathbf{x}), \delta(\mathbf{x})] \quad (19)$$

subject to:  $g(\mathbf{x}) < 0$ .

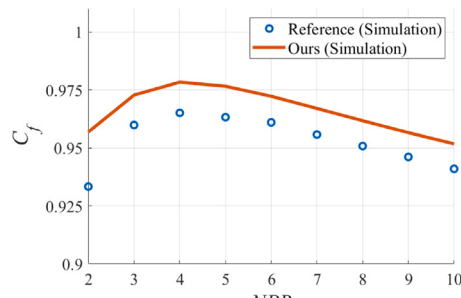
$$g(\mathbf{x}) = \begin{bmatrix} g_1 \\ g_2 \end{bmatrix} = \begin{bmatrix} C_{f,\text{baseline}} - C_f \\ \delta_{\text{baseline}} - \delta \end{bmatrix}$$

where  $\mathbf{x}$  is the shape parameters.

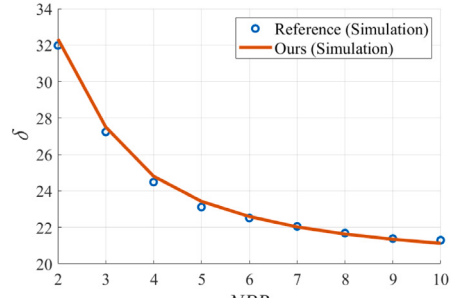
### 3.2. Validation of CFD analysis

To validate the reliability of the CFD analysis, the calculation results for the baseline configuration were compared with those from the study conducted by Gu et al. [29]. Numerical simulations were performed using the FLUENT 2024 R2 software [48]. Fig. 4(a) presents the comparison of the thrust ratio as a function of NPR with the reference data, while Fig. 4(b) shows the comparison of the deflection angle as a function of NPR with the reference data. Both validation results demonstrate average error rates of 0.72% and 1.35%, respectively, confirming the accuracy of the flow solutions. The slight differences observed are attributed to the influence of the rounding radius in the nozzle geometry. In the reference study validated in this work [29], the bottom throat rounding radius was reported, but the details regarding other rounding radii were not provided. This lack of information likely altered the physical flow phenomena inside the nozzle compared to the original configuration. The effects of rounding radii on nozzle performance and flow behavior have been comprehensively studied and summarized in [40].

Additionally, a Grid independence test was conducted to evaluate grid sensitivity. The results revealed that the difference in the thrust



(a) Reference vs. Ours (Thrust ratio).



(b) Reference vs. Ours (Deflection angle).

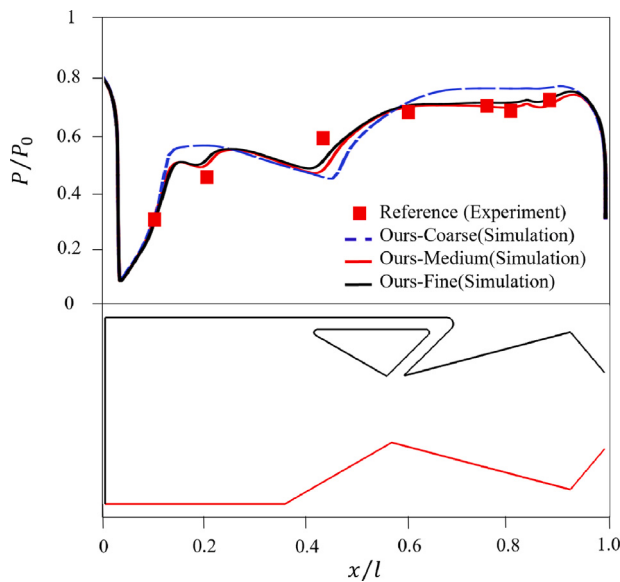
Fig. 4. Validation of thrust ratio ( $C_f$ ) and deflection angle ( $\delta$ ) with respect to NPR.

Fig. 5. Validation of pressure distribution along the lower wall of the BDTN at the design NPR condition (NPR = 3).

ratio between the medium and fine grids was 0.139%, while the difference in the thrust vectoring angle was 0.073%, with both performance metrics exhibiting errors within approximately 0.1%. Based on these results, the medium grid was ultimately selected, considering both efficiency and accuracy (Table 2).

At the design condition of  $NPR = 3$ , the pressure distribution along the lower wall of the nozzle was also validated against experimental data (Fig. 5). The figures confirm a high degree of agreement with the experimental data, verifying the reliability of the simulation. Furthermore, the results of the Grid independence test include surface pressure distributions along the cavity lower wall for coarse, medium, and fine grids. The figures demonstrate that the surface pressure differences between the medium and fine grids are negligible, confirming the validity of selecting the medium grid.

### 3.3. A parameter study by finite differencing

To evaluate the effects of the eight design parameters on the thrust ratio ( $C_f$ ) and thrust vector angle ( $\delta$ ), a sensitivity analysis was conducted using the finite difference method (FDM). Each parameter was varied independently while the remaining parameters are fixed.

Fig. 6 presents the performance trends of  $C_f$  and  $\delta$  as a function of each varying parameter. Additionally, Fig. 7 through Fig. 15 provide Mach number contour plots corresponding to the minimum,

baseline, and maximum values within the selected parameter bounds. The baseline configuration is indicated in red.

In general, when the nozzle flow becomes slightly overexpanded due to the selected shape parameters, a decrease in  $C_f$  and an improvement in  $\delta$  are observed. The reduction in  $C_f$  is attributable to energy loss induced by the shockwave, as described in Eq. (20), while the improvement in  $\delta$  is caused by the formation of a high-pressure region in the cavity due to the shockwave.

$$\frac{p_{01}}{p_0} = \left[ \frac{2\gamma M_2^2 - (\gamma - 1)}{(\gamma + 1)M_2^2} \right]^{\frac{1}{\gamma-1}} \quad (20)$$

Fig. 6(a) and Fig. 7 show the effect of varying the upstream convergent angle ( $\theta_1$ ). The nozzle thrust ratio decreases sharply as  $\theta_1$  increases. This sharp drop is attributed to the formation of a Prandtl-Meyer expansion fan, as described by (21), which lowers the pressure. As  $\theta_1$  increases, the Prandtl-Meyer expansion region enlarges, further reducing the flow pressure, as indicated by the sonic line in the figure. To compensate for this reduced pressure, a shock wave forms, and stronger shock waves occur when there is a larger pressure difference to offset. Consequently, as  $\theta_1$  increases, the thrust ratio decreases. However, due to complex physical phenomena, the deflection angle does not exhibit a clear trend.

$$v(M) = \sqrt{\frac{\gamma+1}{\gamma-1}} \tan^{-1} \left( \sqrt{\frac{\gamma-1}{\gamma+1}} (M^2 - 1) \right) - \tan^{-1} \left( \sqrt{M^2 - 1} \right) \quad (21)$$

$$v_2 = v_1 + \theta_1 \quad (22)$$

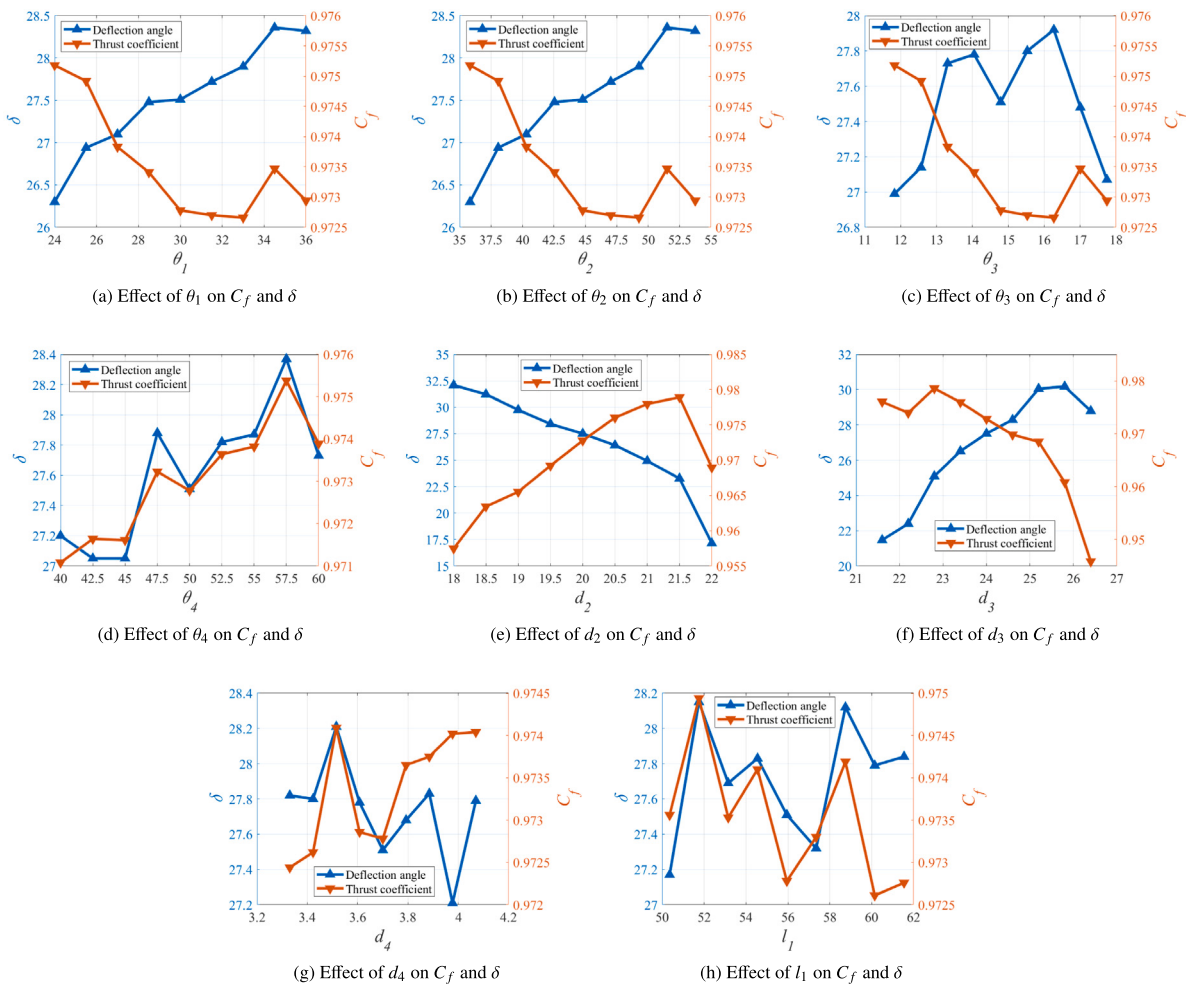
Here,  $v_1$  represents the flow angle before the expansion, while  $v_2$  corresponds to the angle after the expansion.

The Fig. 6(b) and Fig. 8 illustrates the effect of the bypass injection angle. As  $\theta_2$  increases, the area where the primary flow interacts with the wall expands, resulting in a greater deflection and an increase in the deflection angle. In contrast, the thrust ratio decreases due to the choking in the upstream throat caused by the injection flow acting as a wall, which induces additional losses. However, when  $\theta_2$  exceeds 50–52 degrees, the opposing momentum of the injection flow decreases, leading to an increase in the thrust ratio.

Fig. 6(c), and Fig. 9 and Fig. 6(d), and Fig. 10 illustrate the effects of the diverging angle and converging angle of the cavity area, respectively. As  $\theta_3$  increases, both the thrust ratio and deflection angle show similar trends of increase and decrease. When  $\theta_3$  is small, the effective area through which the flow passes is reduced, leading to poor performance due to strong shock waves. However, once  $\theta_3$  exceeds a certain value, an excessively large cavity separation bubble disrupts the primary flow, resulting in suboptimal performance.

As  $\theta_4$  increases, performance improves. This suggests that a compact distribution of high-pressure regions within the cavity, rather than a wide distribution, positively impacts performance.

Fig. 6(e) and Fig. 11 show the effects of the upstream height of the throat area. As  $d_2$  decreases, the flow area narrows, leading to an

Fig. 6. Effect of parameters on  $C_f$  and  $\delta$ .

increase in flow momentum. This increased momentum causes stronger shock formation as the flow compensates for the reduced pressure, resulting in higher pressure losses as  $d_2$  decreases. Consequently, the thrust ratio increases as  $d_2$  increases.

However, regarding the thrust vectoring angle, the higher high-pressure region generated in the cavity due to the increased momentum and stronger shockwave when  $d_2$  is smaller enhances the thrust vectoring angle. In an extreme case where  $d_2$  becomes very large, the compact high-pressure region that should be generated by the shockwave instead disperses widely due to the absence of the shockwave, leading to simultaneous reductions in both nozzle thrust and vectoring performance (see Fig. 12 for pressure contour).

Fig. 6(f) and Fig. 13 illustrates the effects of the downstream throat height,  $d_3$ . As  $d_3$  increases, the flow transitions to an overexpanded state, resulting in the formation of strong shock waves that reduce thrust performance. However, similar to the previously discussed cases, an increase in  $d_3$  leads to a more compact distribution of the high-pressure region, or a very low-pressure region within the cavity's separation bubble, which tends to increase the deflection angle.

The size of the bypass channel was expected to have a significant impact on the mass flow rate, directly influencing the primary flow in the BDTN nozzle. Fig. 6(g) and Fig. 14 illustrates that while an increase in the bypass channel size weakened the shock at the nozzle throat, it did not result in any substantial changes in thrust performance. This is because increasing  $d_4$  does not significantly increase the mass flow rate, which remains almost constant. In fact, when  $d_4$  is smaller, the injection occurs at a higher velocity, generating stronger nonlinear shock waves.

As a result, this leads to a more nonlinear behavior in the thrust ratio and deflection angle.

Fig. 6(h) and Fig. 15 demonstrate the effect of varying the length of the cavity divergence. Although it was expected that the nozzle performance would show a consistent trend with changes in  $l_1$ , no significant performance trend was observed as  $l_1$  varied. This indicates that the key factor in determining performance is not the overall size of the high-pressure and low-pressure separation bubble regions, but rather how strongly and appropriately these regions are positioned.

### 3.4. A parameter study by Shapley function

In this study, SHAP analysis was performed to evaluate the contribution of each design variable to the predictions of both the deflection angle ( $\delta$ ) and the thrust ratio ( $C_f$ ). To perform the SHAP analysis, 83 shapes extracted using the LHS method and 65 shapes used for the sensitivity analysis were used as inputs for SHAP. The SHAP summary plots for these two outputs are shown in Fig. 16(a) and Fig. 16(b), respectively.

The SHAP values quantify the impact of each design variable on the model outputs, where positive SHAP values indicate that a variable increases the predicted output, while negative SHAP values suggest a decrease.

As illustrated in Fig. 16(a), the parameters  $d_2$  and  $d_3$  exhibit the most significant impact on the deflection angle,  $\delta$ . The spread of SHAP values for these parameters indicates a substantial influence on  $\delta$ . For instance, higher values of  $d_2$  tend to decrease  $\delta$ , while larger values

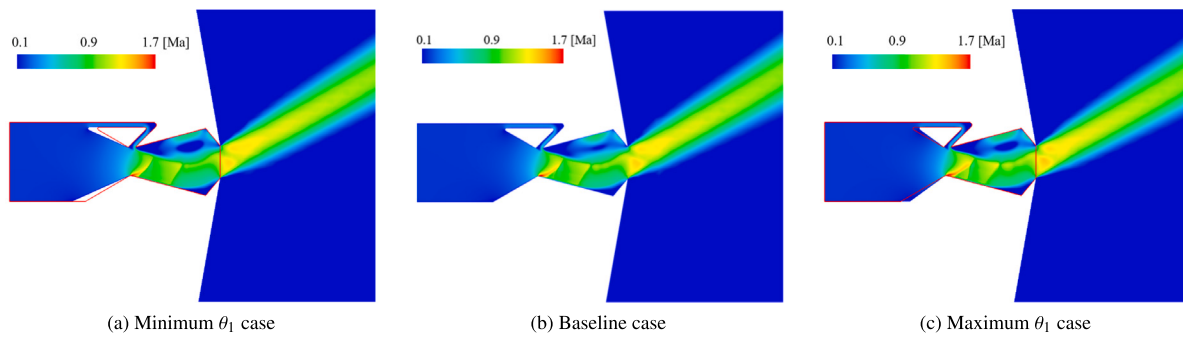


**Fig. 7.** Mach number contour plots for minimum, baseline, and maximum values of  $\theta_1$ .

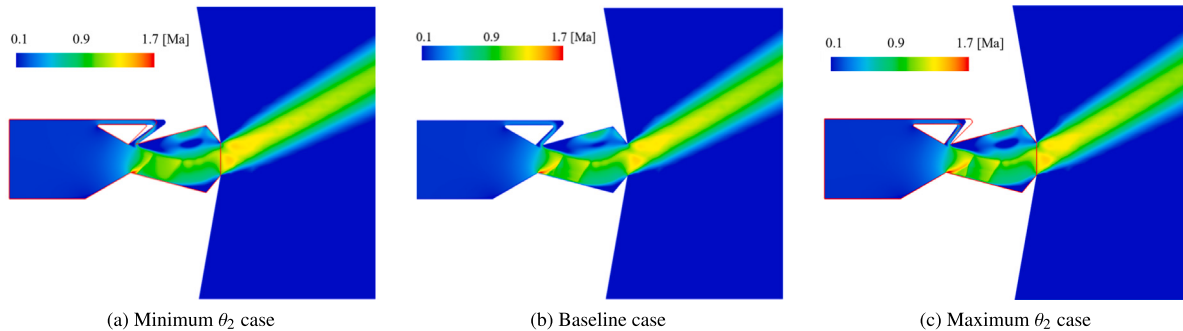


**Fig. 8.** Mach number contour plots for minimum, baseline, and maximum values of  $\theta_2$ .

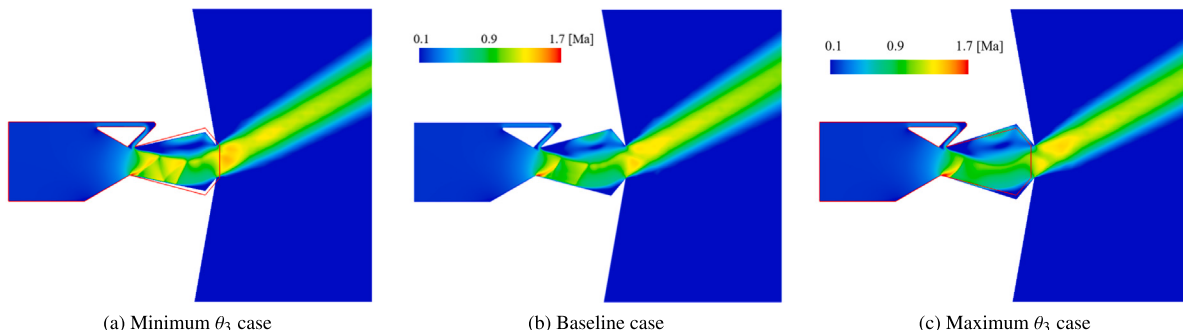


**Fig. 9.** Mach number contour plots for minimum, baseline, and maximum values of  $\theta_3$ .

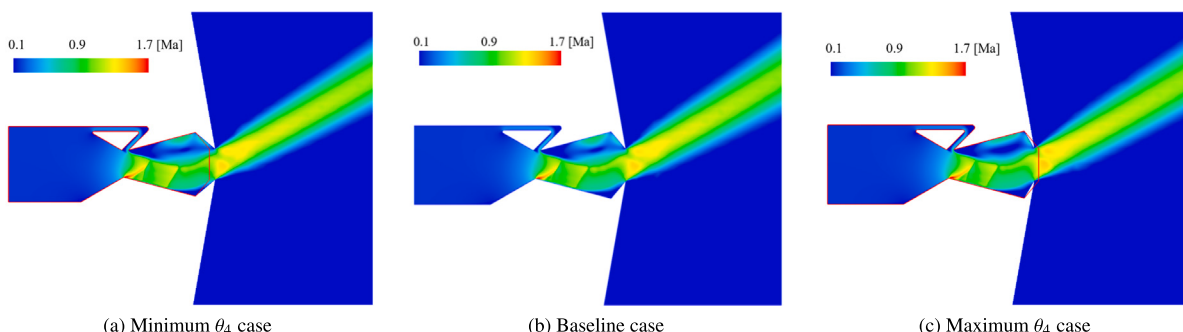


**Fig. 10.** Mach number contour plots for minimum, baseline, and maximum values of  $\theta_4$ .

of  $d_3$  increase it. Other parameters, such as  $\theta_1$  and  $l_1$ ,  $\theta_4$  and  $\theta_2$  also contribute moderately to the deflection angle, whereas  $d_4$ ,  $\theta_3$  show smaller effects, with SHAP values clustering closer to zero.

Regarding the thrust ratio, the SHAP analysis presented in Fig. 16(b) reveals that  $d_2$  and  $d_3$  are again dominant factors. Larger values of  $d_2$  are associated with higher thrust ratio,  $C_f$ , due to the increased

flow area enhancing thrust. Conversely, as  $d_3$  increases, it leads to a reduction in  $C_f$ , possibly due to greater expansion losses. Parameters  $\theta_1$ ,  $\theta_3$ , and  $\theta_4$  demonstrate moderate contributions, while  $d_4$  and  $\theta_2$  have minimal impact on  $C_f$ , as shown by SHAP values near zero.

Both the deflection angle and thrust ratio are strongly influenced by  $d_2$  and  $d_3$ , underlining their critical roles in nozzle performance. The

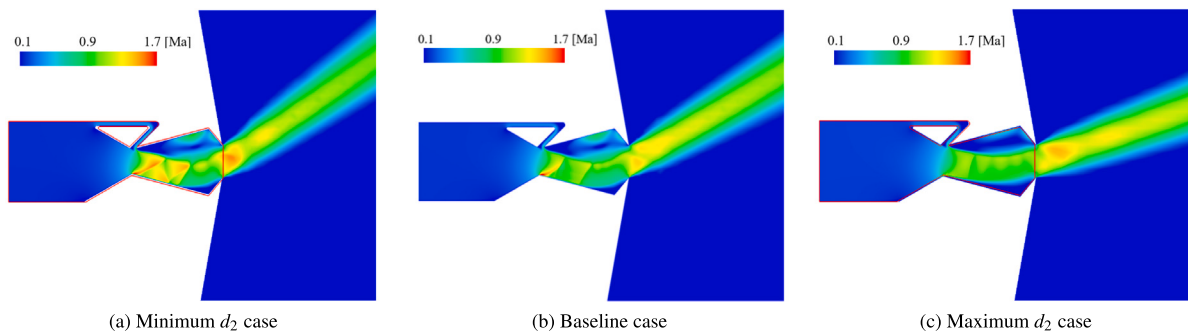


**Fig. 11.** Mach number contour plots for minimum, baseline, and maximum values of  $d_2$ .

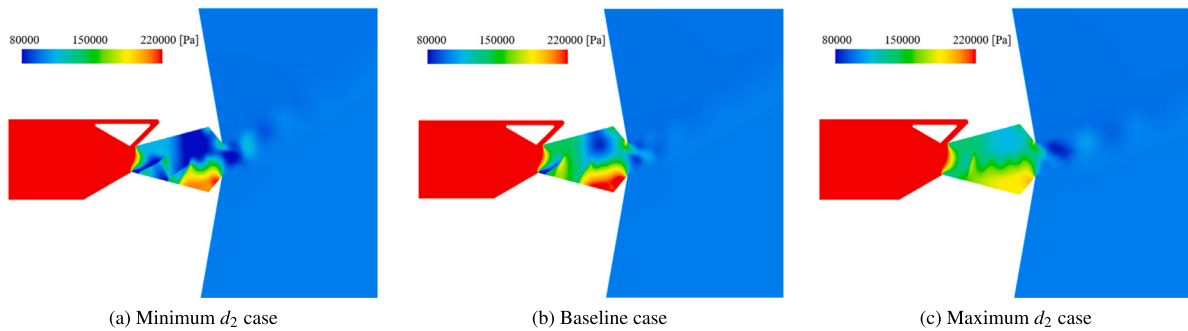


**Fig. 12.** Pressure contour plots for minimum, baseline, and maximum values of  $d_2$ .

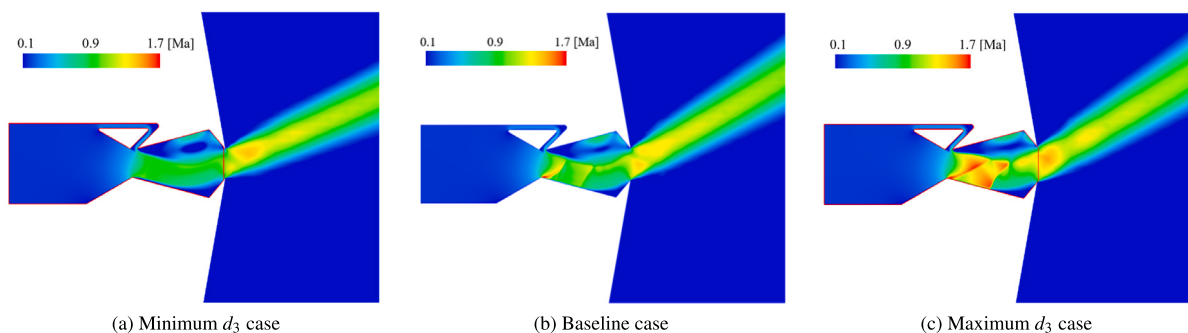


**Fig. 13.** Mach number contour plots for minimum, baseline, and maximum values of  $d_3$ .

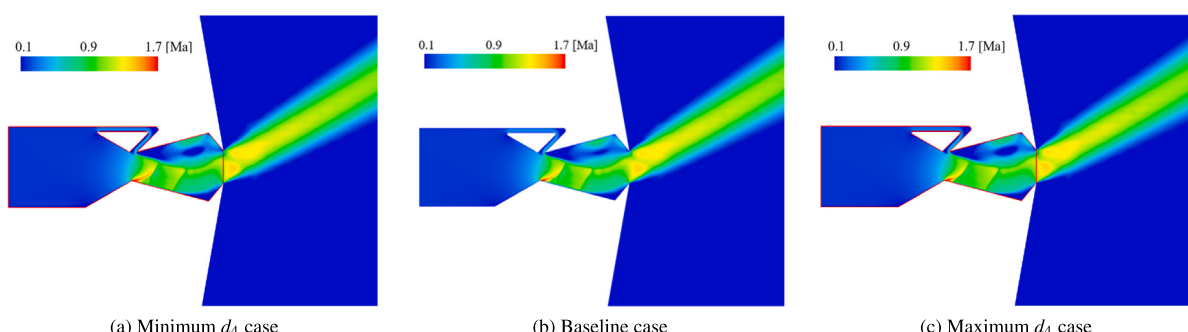


**Fig. 14.** Mach number contour plots for minimum, baseline, and maximum values of  $d_4$ .

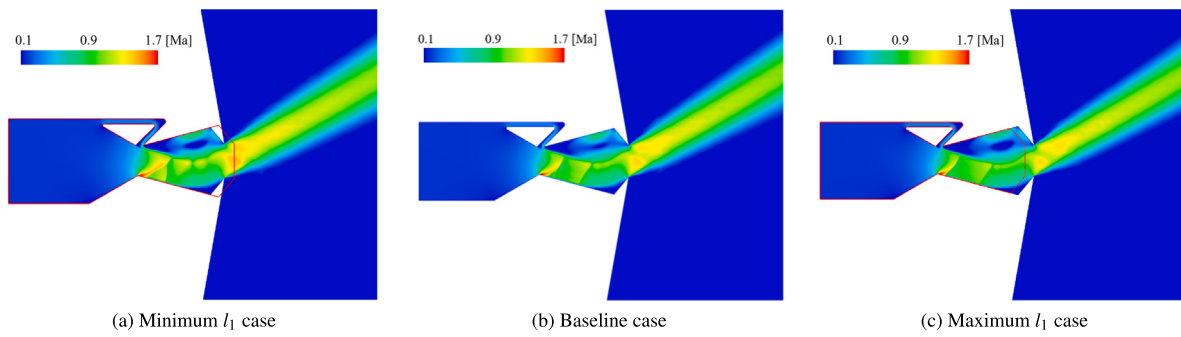


**Fig. 15.** Mach number contour plots for minimum, baseline, and maximum values of  $l_1$ .

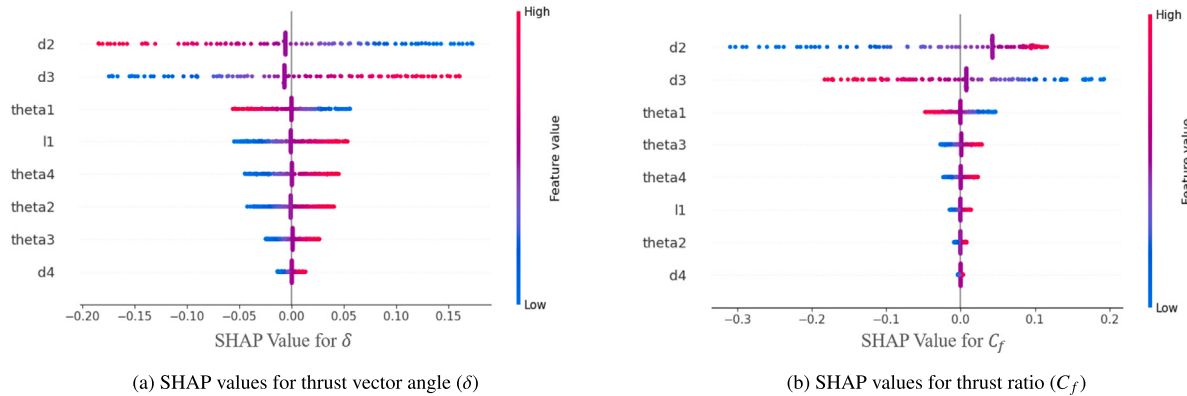


**Fig. 16.** SHAP analysis results for thrust vector angle and thrust ratio.

variable  $d_2$  influences the effective flow area, directly impacting thrust and deflection efficiency. Meanwhile,  $d_3$ , by altering the downstream throat height, affects both shock formation and pressure distribution, thereby playing a crucial role in achieving an optimal balance between thrust and thrust vectoring performance.

#### 4. Design applications

---

##### Algorithm 1 Optimization procedure.

---

- 1: **Input:** Shape parameters generated through LHS
  - 2: **Step 1: CFD Simulations**
  - 3: Perform CFD simulations on the shape parameters obtained from LHS to compute the thrust ratio ( $C_f$ ) and deflection angle ( $\delta$ ).
  - 4: **Step 2: Train GPR Surrogate Model**
  - 5: Use the CFD simulation results to train a GPR model. The surrogate model will predict  $C_f$  and  $\delta$  for new shape parameters.
  - 6: **Step 3: Optimize using gradient free method**
  - 7: Apply the genetic algorithm to identify the Pareto front for  $C_f$  and  $\delta$ .
  - 8: **Return:** Optimal shape parameters  $x$  for the desired performance coefficient (Pareto front for  $C_f$  and  $\delta$ )
- 

#### 4.1. Design optimization procedure

The process for optimizing nozzle performance is as follows. A surrogate model was developed using a Gaussian Process Regression (GPR) approach. The training dataset consisted of 83 shape cases generated through Latin Hypercube Sampling (LHS) to ensure uniform coverage of the design space, and 65 additional cases derived from sensitivity analysis to enhance the diversity of the dataset. The data was split into training and test sets, reserving 10% of the data for testing.

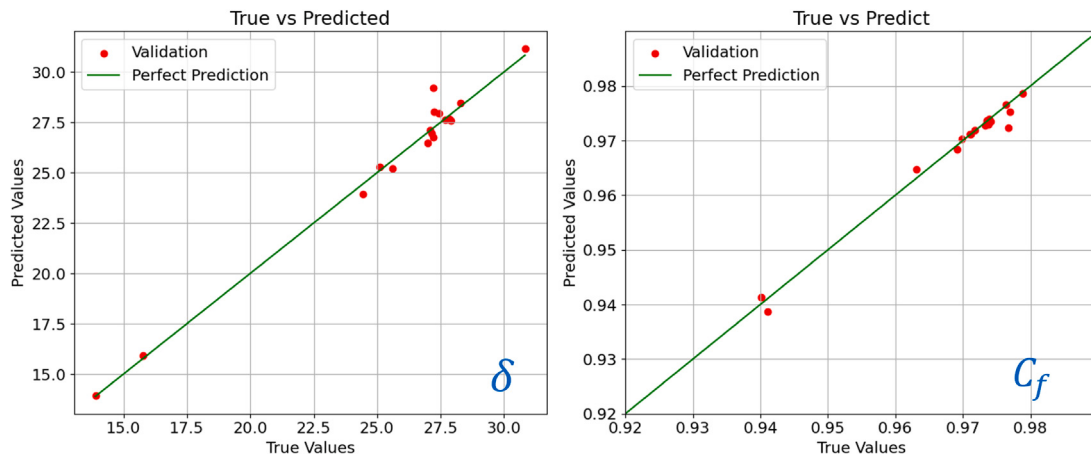
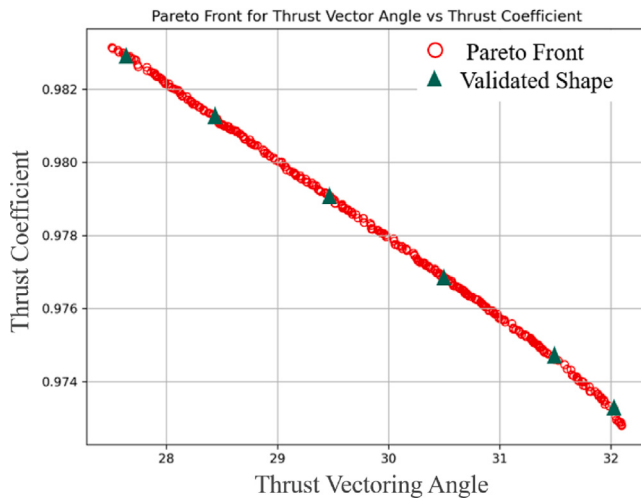
The GPR model employed a Radial Basis Function (RBF) kernel to capture nonlinear relationships between the design variables and performance metrics ( $C_f$  and  $\delta$ ). Hyperparameters were optimized using maximum likelihood estimation (MLE), and the model was evaluated using cross-validation. The GPR model achieved mean error rates of 0.15% for  $C_f$  and 2.32% for  $\delta$ , indicating high predictive accuracy. The agreement between predicted and true values is illustrated in Fig. 17, demonstrating the model's effectiveness in capturing the complex relationships within the design space.

The continuous GPR model is then optimized using the NSGA-II, a multi-objective optimization algorithm, to derive optimized shapes. This process is summarized in Algorithm 1. The optimization process generated a Pareto front, which represents the trade-off relationship between the two objective functions. As shown in Fig. 18, the Pareto front effectively visualizes this trade-off.

Subsequently, Pareto solutions were validated with CFD simulations. The results of the validated solutions are listed in Table 3. The average relative errors were 2.66% and 0.22% for the thrust vector angle and thrust ratio, respectively. Among the six optimized solutions, thrust vector angle improvements ranged from 27.26 degrees to 31.04 degrees, representing a maximum improvement of 12.83% compared to the baseline. Thrust ratio improvements ranged from 0.972 to 0.979, achieving a maximum improvement of 0.70% compared to the baseline. A trade-off relationship between the improvement in angle and thrust ratio was observed. Therefore, the appropriate shape should be selected based on the priority given to each objective during the shape design process.

#### 4.2. Discussion of design results

Detailed values for each shape are expressed as relative displacements from the baseline in percentage terms, as shown in Table 4. In particular,  $\theta_1$  is significantly reduced in all optimized shapes compared to the baseline. As  $\theta_1$  increases, a Prandtl-Meyer expansion fan enlarges,

Fig. 17. True vs. Predicted values for deflection angle  $\delta$  and thrust ratio  $C_f$ .Fig. 18. Pareto front derived from optimization of  $C_f$  and  $\delta$  for various BDTN configurations.

**Table 3**  
Pareto and validated results of thrust vector angle and thrust ratio.

	Pareto		Validated	
	Angle [deg]	$C_f$	Angle [deg]	$C_f$
Optimized shape #1	27.52	0.983	27.26	0.979
Optimized shape #2	28.51	0.981	28.04	0.979
Optimized shape #3	29.51	0.979	28.77	0.976
Optimized shape #4	30.54	0.977	29.63	0.975
Optimized shape #5	31.53	0.975	30.07	0.972
Optimized shape #6	32.10	0.973	31.04	0.973

resulting in a reduction in flow pressure. This creates a shock wave in the cavity as the flow attempts to equalize with atmospheric pressure, which subsequently decreases  $C_f$ . Consequently, the shock waves within the cavity of the optimized shapes are reduced compared to the baseline, which is why reducing the  $\theta_1$  value was chosen as an optimal parameter adjustment.

For  $\theta_2$ , the optimized shape configuration shows an increase in the positive direction compared to the baseline. In previous sections, we observed that an increase in  $\theta_2$  enhances the thrust vectoring angle. Although a higher  $\theta_2$  causes a decrease in the thrust ratio due to choked flow in the upstream throat area from the larger interaction region with the primary flow, the optimized shapes show that the chosen  $\theta_2$  value

improves both the thrust vectoring angle and thrust ratio relative to the baseline, yielding an optimal configuration.

$\theta_3$ , which controls the cavity diverging angle, does not show a distinct trend. However, beyond a certain threshold, both the thrust vectoring angle and thrust ratio exhibit increases or decreases depending on the value of  $\theta_3$ . Thus, an optimal value for  $\theta_3$  was chosen to provide higher thrust vectoring and thrust ratio compared to the baseline while avoiding the performance reduction associated with a larger separation bubble.

$\theta_4$  demonstrates a trend where increasing it results in an improvement in both the thrust vectoring angle and thrust ratio. Accordingly, the optimal value for  $\theta_4$  is found near the maximum allowable range. This occurs because increasing the downstream converging angle generates a compact high-pressure region that positively impacts thrust performance.

$d_2$ , representing the upstream throat area, exhibits a clear trade-off relationship between the thrust vectoring angle and thrust ratio. Decreasing  $d_2$  increases flow momentum, creating a strong shock wave within the nozzle cavity that reduces the thrust ratio. However, the resulting high-pressure region in the nozzle increases the thrust vectoring angle. Therefore, the optimal value for  $d_2$  is selected to balance both performance metrics without compromising either.

$d_3$ , the downstream throat height, increases shock wave complexity within the flow as it grows, which in turn reduces the thrust ratio due to pressure losses. Conversely, an increase in shock waves generates a larger high-pressure region within the cavity, enhancing the thrust vectoring angle. Since  $d_3$  has a strong trade-off effect, the optimal value is positioned near the baseline, requiring careful selection based on flow objectives and design requirements, as  $d_3$  is a sensitive parameter.

Variations in  $d_4$  do not substantially affect the thrust vectoring angle or thrust ratio. However, a narrow bypass channel increases the flow velocity into the primary flow, which could induce nonlinear shock waves and lead to unstable flow. Thus, an optimal value for  $d_4$  greater than the baseline was selected, which provides better thrust vectoring and ratio.

The parameter  $l_1$ , which represents the cavity diverging length, was intended to control the size of the high-pressure region. However, it did not exhibit a clear trend in terms of impact on performance. Nonetheless, analysis of Mach number contours indicates that when  $l_1$  is longer, the shock waves within the cavity are reduced compared to a shorter  $l_1$ . Although  $l_1$  did not produce a strong performance trend in terms of thrust vectoring angle and thrust ratio, a value near the maximum boundary was selected as optimal for stable flow by reducing shock wave formation.

The performance changes across the optimized shape parameters consistently show that reducing  $\theta_1$  and increasing  $\theta_2$ ,  $\theta_4$ , and  $l_1$  improves performance. Fig. 19 presents the Mach number contours for the

**Table 4**

Design parameter variations for optimized shapes compared to baseline (% change).

Parameter	$\theta_1$ [deg]	$\theta_2$ [deg]	$\theta_3$ [deg]	$\theta_4$ [deg]	$d_2$ [mm]	$d_3$ [mm]	$d_4$ [mm]	$l_1$ [mm]
Optimized shape #1	-19.947	19.998	4.092	19.834	0.786	-1.546	9.344	9.977
Optimized shape #2	-19.944	19.274	6.057	19.947	0.755	-0.064	9.313	9.987
Optimized shape #3	-19.692	19.992	10.009	19.901	0.911	1.719	9.719	9.964
Optimized shape #4	-19.932	19.878	16.596	19.975	1.500	4.176	9.008	9.867
Optimized shape #5	-19.932	19.965	18.464	19.989	1.552	5.822	9.014	9.971
Optimized shape #6	-19.823	19.983	16.739	19.356	1.748	6.944	7.883	9.954

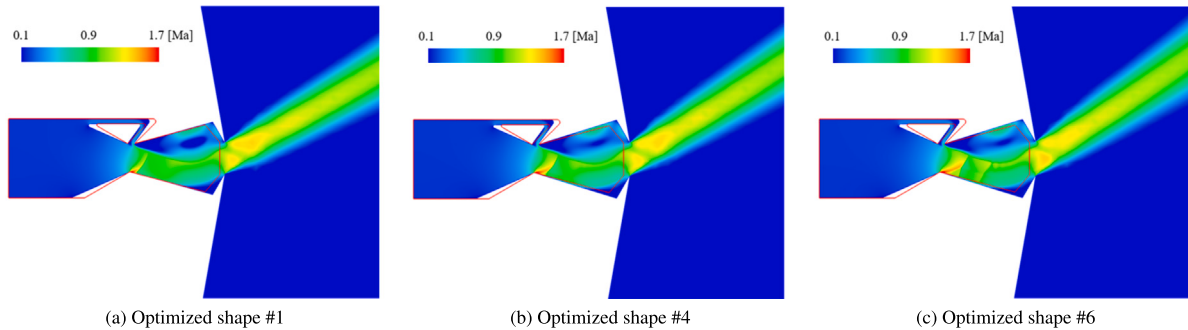


Fig. 19. Mach number contours for the optimized nozzle shapes.

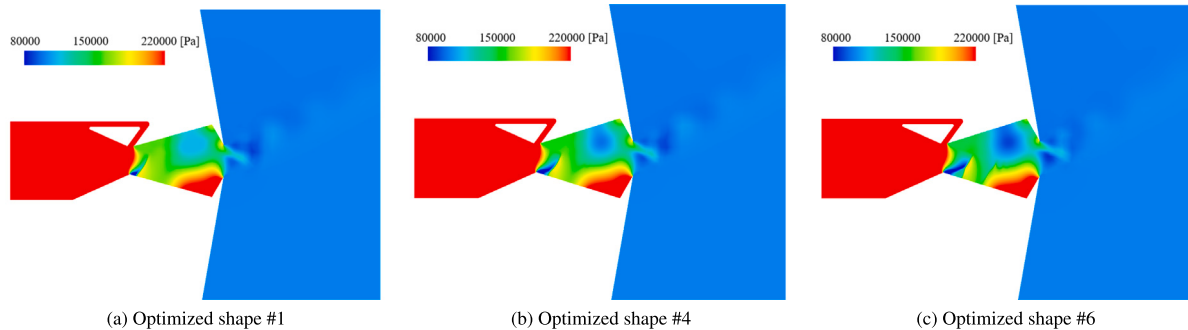


Fig. 20. Pressure contours for the optimized nozzle shapes.

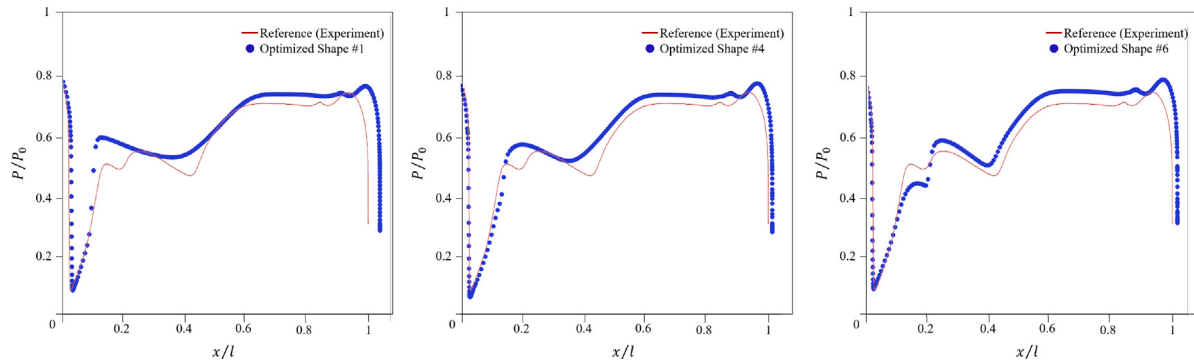


Fig. 21. Surface pressure distribution along the lower cavity for optimized shapes #1, #4, and #6.

optimized shapes, compared with the baseline configuration, showing substantial changes in the optimized designs. As described previously, we can see that  $\theta_1$  is reduced, while  $\theta_2$ ,  $\theta_4$ , and  $l_1$  are increased compared to the baseline. In the case of Optimized Shape #1, which has a high thrust performance, shocks inside the nozzle are minimized, thereby reducing pressure loss. On the other hand, in Optimized Shape #6, where the vectoring angle is maximized, the presence of shock waves in the nozzle creates an appropriate high-pressure region in the cavity, as well as a significant low-pressure region on the upper side of the cavity. These pressure distributions effectively increase the deflection angle. This can be observed in detail in Fig. 20.

Fig. 21 shows the surface pressure in the lower cavity region of the nozzle for Optimized Shapes #1, #4, and #6. In Optimized Shape #1, which optimizes the thrust ratio, there is minimal pressure variation along the lower wall compared to the baseline, as indicated by the surface pressure plot. Additionally, the pressure reduction region due to the expansion fan appears at a position ahead of that in the baseline. In the case of Optimized Shape #6, which maximizes the deflection angle, the lower wall exhibits higher surface pressure than in other optimized shapes. The pressure reduction caused by the expansion fan is similar to that in the baseline, leading to shock formation. The reduced pressure region is located further downstream compared to other

optimized shapes, reaffirming that a compact high-pressure region at an appropriate position within the cavity yields better performance, as demonstrated in the sensitivity analysis.

## 5. Conclusion

This study presents a data-driven approach to optimizing the Bypass Dual Throat Nozzle (BDTN), focusing on enhancing both the thrust ratio ( $C_f$ ) and thrust vector angle ( $\delta$ ). Key insights were obtained through a structured analysis involving sensitivity analysis, SHAP analysis, and optimization.

First, the sensitivity analysis identified several critical shape parameters—namely the upstream convergent angle ( $\theta_1$ ), bypass injection angle ( $\theta_2$ ), cavity divergence angle ( $\theta_3$ ), cavity convergence angle ( $\theta_4$ ), upstream throat height ( $d_2$ ), downstream throat height ( $d_3$ ), bypass duct area height ( $d_4$ ), and cavity divergence length ( $l_1$ ). Variations in these parameters significantly affected BDTN performance, especially in relation to shock wave formation and distribution within the cavity. The parameters  $d_2$  and  $d_3$ , in particular, were found to directly influence flow behavior, with  $d_2$  impacting the flow area and  $d_3$  affecting shock wave structure, both of which are crucial for achieving desired thrust and vectoring efficiencies.

Second, Shapley Additive Explanations (SHAP) analysis was conducted to further quantify the influence of each parameter on BDTN performance. SHAP results indicated  $d_2$  and  $d_3$  as the dominant factors influencing both  $C_f$  and  $\delta$ . Parameters such as  $\theta_1$ ,  $l_1$ ,  $\theta_4$ , and  $\theta_2$  showed moderate contributions, influencing the distribution of high-pressure regions within the cavity. Meanwhile,  $d_4$  and  $\theta_2$  demonstrated smaller impacts on  $C_f$ , with SHAP values clustering closer to zero. These insights enhanced our understanding of the relative importance of each parameter in optimizing nozzle performance.

Finally, optimization was performed using a Gaussian Process Regression (GPR) surrogate model trained on design cases generated through Latin Hypercube Sampling (LHS) and sensitivity analysis data. The GPR model, combined with the multi-objective optimization algorithm, yielded Pareto-optimal shapes balancing  $C_f$  and  $\delta$ . The optimized designs demonstrated significant performance gains, achieving deflection angle improvements of up to 12.83% and thrust ratio increases of 0.70% relative to the baseline. These results confirm the effectiveness of the data-driven approach in balancing thrust performance and vectoring efficiency, achieved by strategically adjusting each parameter to control shock formation within the nozzle cavity.

In summary, this study offers a robust framework for efficiently optimizing BDTN configurations by systematically identifying and adjusting critical shape parameters. Future research could explore adaptive shape adjustments based on real-time flow feedback, potentially advancing BDTN capabilities in fluidic thrust vectoring applications.

## CRediT authorship contribution statement

**Chanho Park:** Writing – review & editing, Writing – original draft, Visualization, Validation, Supervision, Software, Resources, Project administration, Methodology, Investigation, Formal analysis, Data curation, Conceptualization. **Woochan Lee:** Writing – original draft, Visualization, Validation, Software, Resources, Methodology, Investigation, Formal analysis, Data curation. **Seongim Choi:** Writing – review & editing, Supervision, Project administration, Funding acquisition.

## Declaration of competing interest

The authors declare that they have no known competing financial interests or personal relationships that could have appeared to influence the work reported in this paper.

## Acknowledgments

This work was supported by Korea Research Institute for defense Technology planning and advancement (KRIT) grant funded by the Korea government (DAPA(Defense Acquisition Program Administration)) (No. 20-105-E00-005(KRIT-CT-23-010), VTD-32, Performance Analysis and Shape Design Technology for Low Observable, Low Noise Thrust Vectoring Vertical Take-Off and Landing Aircraft, 2024, VTOL Technology Research Center for Defense Applications).

## Data availability

Data will be made available on request.

## References

- [1] Liefer RK, Valasek J, Eggold DP, Downing DR. Fighter agility metrics, research and test. *J Aircr* 1992;29(3):452–7.
- [2] Valasek J, Downing DR. An investigation of fighter aircraft agility. Tech. rep., 1993.
- [3] Harris J, Black G. F-22 control law development and flying qualities. In: 21st atmospheric flight mechanics conference. 1996, p. 3379.
- [4] Neely A, Gesto F, Young J. Performance studies of shock vector control fluidic thrust vectoring. In: 43rd AIAA/ASME/SAE/ASEE joint propulsion conference & exhibit. 2007, p. 5086.
- [5] Wing DJ. Static investigation of two fluidic thrust-vectoring concepts on a two-dimensional convergent-divergent nozzle, vol. 4574, National Aeronautics and Space Administration, Langley Research Center; 1994.
- [6] Anderson C, Giuliano V, Wing D, Anderson C, Giuliano V, Wing D. Investigation of hybrid fluidic/mechanical thrust vectoring for fixed-exit exhaust nozzles. In: 33rd joint propulsion conference and exhibit. 1997, p. 3148.
- [7] Flamm J, Deere K, Mason M, Berrier B, Johnson S. Design enhancements of the two-dimensional, dual throat fluidic thrust vectoring nozzle concept. In: 3rd AIAA flow control conference. 2006, p. 3701.
- [8] Mason M, Crowther W. Fluidic thrust vectoring for low observable air vehicles. In: 2nd AIAA flow control conference. 2004, p. 2210.
- [9] Deere K, Berrier B, Flamm J, Johnson S. Computational study of fluidic thrust vectoring using separation control in a nozzle. In: 21st AIAA applied aerodynamics conference. 2003, p. 3803.
- [10] Afridi S, Khan TA, Shah SIA, Shams TA, Mohiuddin K, Kukulka DJ. Techniques of fluidic thrust vectoring in jet engine nozzles: A review. *Energies* 2023;16(15):5721.
- [11] Deere K. Computational investigation of the aerodynamic effects on fluidic thrust vectoring. In: 36th AIAA/ASME/SAE/ASEE joint propulsion conference and exhibit. 2000, p. 3598.
- [12] Zignonov F, Song M, Sellappan P, Alvi FS. Multiaxis shock vectoring control of overexpanded supersonic jet using a genetic algorithm. *J Propuls Power* 2023;39(2):249–57.
- [13] Wu K, Kim TH, Kim HD. Theoretical and numerical analyses of aerodynamic characteristics on shock vector control. *J Aerosp Eng* 2020;33(5):04020050.
- [14] Abeyounis W, Bennett Jr B. Static internal performance of an over expanded fixed-geometry, nonaxisymmetric nozzle with fluidic pitch-thrust-vectoring capability. In: NASA Paper No. TP-3645. 1997.
- [15] Ferlaudo M, Marsilio R. Numerical investigation of the dynamic characteristics of a dual-throat-nozzle for fluidic thrust-vectoring. *AIAA J* 2017;55(1):86–98.
- [16] Strykowski PJ, Krothapalli A, Forliti D. Counterflow thrust vectoring of supersonic jets. *AIAA J* 1996;34(11):2306–14.
- [17] Deere K. Summary of fluidic thrust vectoring research at NASA langley research center. In: 21st AIAA applied aerodynamics conference. 2003, p. 3800.
- [18] Gu R, Xu J. Effects of cavity on the performance of dual throat nozzle during the thrust-vectoring starting transient process. *J Eng Gas Turbines Power* 2014;136(1):014502.
- [19] Miller D, Yagle P, Hamstra J. Fluidic throat skewing for thrust vectoring in fixed-geometry nozzles. In: 37th aerospace sciences meeting and exhibit. 1999, p. 365.
- [20] Yagle P, Miller D, Ginn K, Hamstra J. Demonstration of fluidic throat skewing for thrust vectoring in structurally fixed nozzles. *J Eng Gas Turbines Power* 2001;123(3):502–7.
- [21] Deere K, Berrier B, Flamm J, Johnson S. A computational study of a dual throat fluidic thrust vectoring nozzle concept. In: 41st AIAA/ASME/SAE/ASEE joint propulsion conference & exhibit. 2005, p. 3505.
- [22] Ferlaudo M, Marsilio R. Numerical simulation of fluidic thrust-vectoring. *Aerotecnica Missili Spazio* 2016;95:153–62.
- [23] Gu R, Xu J. Dynamic experimental investigations of a bypass dual throat nozzle. *J Eng Gas Turbines Power* 2015;137(8):084501.

- [24] Flamm J, Deere K, Berrier B, Johnson S, Mason M. Experimental study of a dual-throat fluidic thrust-vectoring nozzle concept. In: 41st AIAA/ASME/SAE/ASEE joint propulsion conference & exhibit. 2005, p. 3503.
- [25] Shin CS, Kim HD, Setoguchi T, Matsuo S. A computational study of thrust vectoring control using dual throat nozzle. *J Therm Sci* 2010;19:486–90.
- [26] Wu K, Kim TH, Kim HD. Visualization and analysis on the thrust vectoring control in three-dimensional dual-throat nozzles. *J Vis* 2021;24:891–915.
- [27] Flamm J, Deere K, Mason M, Berrier B, Johnson S. Experimental study of an axisymmetric dual throat fluidic thrust vectoring nozzle for supersonic aircraft application. In: 43rd AIAA/ASME/SAE/ASEE joint propulsion conference & exhibit. 2007, p. 5084.
- [28] Deere K, Flamm J, Berrier B, Johnson S. Computational study of an axisymmetric dual throat fluidic thrust vectoring nozzle for a supersonic aircraft application. In: 43rd AIAA/ASME/SAE/ASEE joint propulsion conference & exhibit. 2007, p. 5085.
- [29] Gu R, Xu J, Guo S. Experimental and numerical investigations of a bypass dual throat nozzle. *J Eng Gas Turbines Power* 2014;136(8):084501.
- [30] Zhang Y, Xu J, Pan R, Li Y, Ma Z, Huang S. Numerical investigation of short takeoff and landing exhaust system using bypass dual throat nozzle. *Aerosp Sci Technol* 2023;138:108316.
- [31] Afridi S, Khan TA, Shah I, Ali Y, Mumtaz Qadri MN, Li W. Effect of bypass duct on the thrust vectoring performance of dual throat nozzle in a supersonic aircraft. *J Fluids Eng* 2024;146(6).
- [32] Zhang Y, Jinglei X, Minglei C, Ruifeng P, Huang S. Numerical investigation of dynamic characteristics of dual throat nozzle and bypass dual throat nozzle in thrust vectoring starting process. *Chin J Aeronaut* 2024.
- [33] Bharali S, Joshi S, Zunaid M, et al. Optimization of bypass flow introduction angle in dual-throat nozzle. *J Electr Syst* 2024;20(4s):766–72.
- [34] Hamed-Estakhsar M, Ferlauto M, Mahdavy-Moghaddam H. Numerical study of secondary mass flow modulation in a bypass dual-throat nozzle. *Proc Inst Mech Eng G* 2021;235(4):488–500.
- [35] Pan R, Xu J, Zhang Y, Li Y, Huang S. Numerical simulation and experiment of a bypass dual throat nozzle with tab modification. *Aerosp Sci Technol* 2024;144:108816.
- [36] Huang S, Jinglei X, Kaikai Y, Yangsheng W, Ruifeng P, Kuangshi C, et al. Numerical study of a trapezoidal bypass dual throat nozzle. *Chin J Aeronaut* 2023;36(3):42–62.
- [37] Huang S, Xu J, Yu K, Wang Y, Pan R. Design and experimental study of a bypass dual throat nozzle with the ability of short/vertical takeoff and landing. *Aerosp Sci Technol* 2022;121:107301.
- [38] Kim H, Han D-H, Jin S, Hong J-W. Numerical study of a dual throat bent nozzle using computational fluid dynamics. In: AIAA aviation forum and ascend 2024. 2024, p. 4118.
- [39] Hamed-Estakhsar MH, Mahdavy-Moghaddam H. Experimental evaluation and numerical simulation of performance of the bypass dual throat nozzle. *Proc Inst Mech Eng G* 2021;235(7):768–81.
- [40] Wang Y, Xu J, Huang S, Lin Y, Jiang J. Computational study of axisymmetric divergent bypass dual throat nozzle. *Aerosp Sci Technol* 2019;86:177–90.
- [41] Wang Y, Xu J, Huang S, Jiang J, Pan R. Design and preliminary analysis of the variable axisymmetric divergent bypass dual throat nozzle. *J Fluids Eng* 2020;142(6):061204.
- [42] Wu K, Kim H. A fluidic thrust vector control using the bypass flow in a dual throat nozzle. *J Mech Sci Technol* 2021;35(8):3435–43.
- [43] Huang S, Ruifeng P, Jinglei X, Gu R, Zhang Y. A parametric investigation of dual-throat nozzle bypass channel configurations for advanced aviation applications. *Helijon* 2024.
- [44] Park C, Choi S. Dual throat nozzle shape optimization using AI. In: Proceedings of the Korean society of computational fluid engineering conference. 2023.
- [45] Shih T-H, Liou WW, Shabbir A, Yang Z, Zhu J. A new  $k-\epsilon$  eddy viscosity model for high reynolds number turbulent flows. *Comput & Fluids* 1995;24(3):227–38.
- [46] Mangalathu S, Hwang S-H, Jeon J-S. Failure mode and effects analysis of RC members based on machine-learning-based SHapley Additive exPlanations (SHAP) approach. *Eng Struct* 2020;219:110927.
- [47] Gramacy RB. Surrogates: Gaussian process modeling, design, and optimization for the applied sciences. Chapman and Hall/CRC; 2020.
- [48] Matsson JE. An introduction to ansys fluent 2023. Sdc Publications; 2023.